



1

2 **Towards an objective assessment of climate multi-model**
3 **ensembles. A case study in the Senegalo-Mauritanian upwelling**
4 **region**

5 Juliette Mignot¹, Carlos Mejia¹, Charles Sorrow¹, Adama Sylla^{1,2}, Michel Crépon¹ and Sylvie
6 Thiria^{1,3}.

7 ¹ IPSL-LOCEAN, SU/IRS/CNRS/MNHN, Paris, France

8 ² LPAO-SF, ESP, UCAD, Dakar, Sénégal

9 ³ UVSQ, F-78035, Versailles, France

10 *Correspondence to:* Juliette Mignot (Juliette.mignot@locean-ipsl.upmc.fr)

11 **Abstract.** Climate simulations require very complex numerical models. Unfortunately, they
12 typically present biases due to parameterizations, choices of numerical schemes, and the
13 complexity of many physical processes. Beyond improving the models themselves, a way to
14 improve the performance of the modeled climate is to consider multi-model averages. Here, we
15 propose an objective method to select the models that yield an efficient multi-model ensemble
16 average. We used a neural classifier (Self-Organizing Maps), associated with a multi-
17 correspondence analysis to identify the models that best represent some target climate property.
18 One can then determine an efficient multi-model ensemble. We illustrate the methodology with
19 results focusing on the mean sea surface temperature seasonal cycle over the Senegalo-
20 Mauritanian region. We compare 47 CMIP5 model configurations to available observations. The
21 method allowed us to identify a performing multi-model ensemble by averaging 12 climate
22 models only. Future behavior of the Senegalo-Mauritanian upwelling was then assessed using
23 this multi-model ensemble.

24 **1- Introduction**

25 In this study we present a methodology aiming at selecting a coherent sub-ensemble of the
26 models involved in the 5th Climate Model Intercomparison Project (CMIP5) that best represents
27 specific observed characteristics. The analysis is performed on the capacity of the models to



28 represent the seasonal cycle of the sea surface temperature (SST) in the region of the Senegalo-
29 Mauritanian upwelling off the west coast of Africa.

30 The Senegalo-Mauritanian upwelling has focused increasing attention over the recent
31 years. It presents an important seasonal cycle associated with mesoscale patterns whose
32 variability has been recently studied by several oceanographic campaigns (Capet et al., 2017;
33 Faye et al., 2015; Ndoye et al., 2014). The very productive waters associated with the upwelling
34 have a strong economic impact on fisheries in Senegal and Mauritania, and a crucial societal
35 importance for local populations. It is therefore of importance to predict the evolution of the
36 dynamics and the physics of the upwelling in the forthcoming decades due to the effect of climate
37 warming and its consequences on biological productivity which may impact the fisheries. The
38 most common way to predict the evolution of the climate is to run climate models, which include
39 fully coupled atmosphere-ocean-cryosphere-biosphere modules. Because of their quite low
40 resolution and the fact that they use different parameterizations of the physics, numerical
41 schemes and sometimes include or neglect different processes, these models have some marked
42 biases in specific regions. They also have different responses to an imposed increase of
43 atmospheric greenhouse gases, which partly explain their mean climate biases. This variety of
44 models allows us to assess the uncertainty of present climate representation when compared to
45 observations and, by studying their dispersion, to roughly estimate the uncertainty of the response
46 to future climate change. For several generations of climate models, it has been shown that the
47 multi-model average for a variety of variables mostly agrees better with observations of present
48 day climate than any single model, and that the average also consistently scores higher in almost
49 all diagnostics (Gleckler et al., 2008; Lambert and Boer, 2001; Phillips and Gleckler, 2006;
50 Pincus et al., 2008; Reichler and Kim, 2008; Santer et al., 2009; Tebaldi and Knutti, 2007).
51 Several studies also suggest that the most reliable climate projection is given by a multi-model
52 averaging (Knutti et al., 2010), rather than averaging different projections performed with a
53 single model run with different initial conditions for example. This result relies on the assumption
54 that if choices of parameterizations, specific numerical schemes, are made independently for each
55 model, then the errors might at least partly compensate, resulting in a multi-model average that is
56 more skillful than its constitutive terms (Tebaldi and Knutti, 2007). The significant gain in
57 accuracy can be explained by the fact that the errors specific to each model compensate each
58 other in the averaging procedure used to build the multi-model. However, the number of GCMs



59 available for climate change projections is increasing rapidly. For example, the CMIP5 archive
60 (Taylor et al., 2012), which was used for the fifth IPCC Assessment Report (IPCC, 2013),
61 contains outputs from 61 different GCMs and 70 contributions are expected for CMIP6.
62 Nevertheless, these models constitute a fully independent ensemble (e.g. (Masson and Knutti,
63 2011). It thus becomes possible and probably needed to select and/or weight the models
64 constituting such an average. Recent work has suggested that weighting the multi-model
65 averaging procedure could help to reduce the spread and thus uncertainty of future projections.
66 Such an approach has been applied extensively to the issue of climate sensitivity (Fasullo and
67 Trenberth, 2012; Gordon et al., 2013; Huber and Knutti, 2012; Tan et al., 2016). Valuable
68 improvement of models selection has also been found in studies of the carbon cycle (Cox et al.,
69 2013; Wenzel et al., 2014), the hydrological cycle (Deangelis et al., 2015; O’Gorman et al.,
70 2012), the Antarctic atmospheric circulation (Son et al., 2010; Wenzel et al., 2016), extratropical
71 atmospheric rivers (Gao et al., 2016), atmospheric and ocean heat transports (Loeb et al., 2015),
72 the European temperature variability (Stegehuis et al., 2013) and temperature extremes (Borodina
73 et al., 2017).

74 The present paper is dedicated to the elaboration of an objective method to select models
75 according to their performance over the Senegalo-Mauritanian upwelling region, with the aim of
76 constructing an efficient climate multi-model average together with its related confidence interval
77 in order to anticipate the effect of climate warming by the end of the century in this region. This
78 upwelling is very intense and presents a well-marked seasonal variability. Its intensity is stronger
79 in boreal winter and it disappears in summer with the northward progression of the ITCZ. Due to
80 the enrichment of the sea surface layers with nutrients upwelled from deep layers, it drives an
81 important phytoplankton bloom that is observed on ocean color satellite images (Demarcq and
82 Faure, 2000; Farikou et al, 2015). The maximum intensity of this bloom occurs in March-April
83 (Farikou et al., 2015; Faye et al., 2015; Ndoye et al., 2014). This upwelling lies at is the southern
84 end of the Canarian upwelling system. North of 20°N, which is the northernmost latitude reached
85 by the ITCZ, the seasonality of the upwelling is much weaker. It is forced by the trades, which
86 are more intense in summer. Consequently, the Senegalo-Mauritanian upwelling is characterized
87 by a very specific seasonality which is observed on satellite SST (Demarcq and Faure, 2000;
88 Sawadogo et al., 2009). Sylla *et al.* (2019) have recently showed that the intensity of the SST



89 seasonal cycle along the coast of Senegal and Mauritania was a good marker of the upwelling in
90 climate models.

91 The paper is articulated as follows: section 2 presents the different climate models and
92 the climatological observations used in the study, together with the region of interest. The
93 classification method is described in section 3 for the extended region and results are discussed.
94 Section 4 investigates the results of the method applied over a smaller area, more focused over
95 the region of interest. Section 5 uses the two multi-model clusters defined in sections 3 and 4
96 respectively to describe the representation of the Senegalo-Mauritanian upwelling and its change
97 under global warming. Conclusions are given in section 6.

98 **2- Models and region of interest**

99 **2.1 Data**

100 This study is based on the CMIP5 (Coupled Model Inter-comparison Project Phase 5) database.
101 We used the output of the 47 simulations listed in Table 1. The models have been evaluated over
102 the historical period defined as [1975-2005] by comparing their output to observations. The mean
103 seasonal cycle of SST over this period is constructed for each model grid point. When several
104 members of historical simulations are available for a same model configuration, they are
105 averaged together. However, this has practically no impact on the estimated mean seasonal cycle
106 (not shown). The mean climatological cycle of the CMIP5 models under study is evaluated
107 against the ERSST_v3b data set (Smith et al., 2008), averaged over the same time period. This
108 data set is used as the target to be reproduced and is denoted "Observation field" hereinafter. In
109 order to deal with data at the same resolution, all model outputs as well a observation fields were
110 been regridded on a 1-degree resolution regular grid prior to analysis.

111 In section 5, the models' selections are used to characterize the response of the upwelling to
112 climate change. This response is characterized in terms of SST but also wind intensity. For this,
113 the simulated wind stress is compared to the QUICKSCAT product (<https://podaac.jpl.nasa.gov>)
114 and the models are evaluated over the period [1985-2005].

115

116 **2.2 The Senegalo-Mauritanian upwelling region**



117 In the present research, we evaluated the ability of the different climate models to represent the
118 Senegalo-Mauritanian upwelling. Following Sylla et al. (in rev.), we consider the intensity of the
119 seasonal cycle of the SST as a marker of the upwelling variability and localization. This variable
120 is shown in Fig. 1 for the eastern tropical Atlantic. This figure confirms that the Senegalo-
121 Mauritanian coast stands out with a very strong seasonal SST cycle as compared to what is found
122 at similar latitudes in the open ocean. This results from the cold SST generated by the strong
123 winds occurring in winter. The Senegalo-Mauritanian upwelling is confined in a small region of
124 the order of 100km off the western coast of Africa. It is part of a complex and fine scale regional
125 circulation system recently revisited by Kounta *et al.*, (2018). Since the grid mesh of most of the
126 climate models is of the order of 1° ($\sim 100\text{km}$), this regional circulation is thus poorly resolved,
127 and this pleads for a relatively large-scale analysis of the upwelling representation in climate
128 models. The Senegalo-Mauritanian upwelling is also embedded in a large scale oceanic
129 circulation pattern, encompassing the North Equatorial Counter Current flowing eastward in the
130 southern part of the region and the return branch of the subtropical gyre in the northwestern part.
131 Therefore, we will firstly study the representation of the SST seasonal cycle intensity in the
132 different climate models over a relatively large region that includes part of the Canary current in
133 the North and the Guinea dome in the South. The so-called “extended region” is defined by a
134 rectangular box extending from 9°W to 45°W and from 5°N to 30°N (Fig. 1). In a second step,
135 we will proceed to the same analysis and classification of the models within a much more
136 focused (hereafter zoomed) region, namely [16°W - 28°W and 10°N - 23°N] (Fig. 1). All the results
137 below will be first shown for the extended region. Comparison with the focused region will be
138 done in section 4.

139 **3 - Classification of the climate models over the extended upwelling region**

140 **3.1 The methodological approach**

141 The first step of the methodology is to decompose the selected region in different classes by
142 using a neural network classifier, the so-called Self Organizing Map (SOM; Kohonen, 2013).
143 This algorithm constitutes a powerful nonlinear unsupervised classification method. It has been
144 commonly used to solve environmental problems (Hewitson and Crane, 2002; Jouini et al., 2013,
145 2016; Liu et al., 2006; Reusch et al., 2007; Richardson et al., 2003). The SOM aims at clustering
146 vectors of a multidimensional database (D) into classes represented by a fixed network of



147 neurons (the SOM map). The self-organizing map (SOM-map) is defined as an undirected graph,
148 usually a 2D rectangular grid. This graphical structure is used to define a discrete distance
149 (denoted by δ) between the neurons of the map and thereby identify the shortest path between
150 two neurons. Moreover, SOM enables the partition of \mathbf{D} in which each cluster is associated with a
151 neuron of the map and is represented by a prototype that is a synthetic multidimensional vector
152 (the referent vector \mathbf{w}). Each vector \mathbf{z} of \mathbf{D} is assigned to the neuron whose referent \mathbf{w} is the
153 closest, in the sense of the Euclidean Norm (EN), and is called the projection of the vector \mathbf{z} on
154 the map. A fundamental property of a SOM is the topological ordering provided at the end of the
155 clustering phase: two neurons that are close on the map represent data that are close in the data
156 space. In other words, the neurons are gathered in such a way that if two vectors of \mathbf{D} are
157 projected on two “relatively” close neurons (with respect to δ) on the map, they are similar and
158 share the same properties. The estimation of the referent vectors \mathbf{w} of a SOM and the topological
159 order is achieved through a minimization process using a learning data set base, here from the
160 observations. The cost function to be minimized is of the form:

$$J_{SOM}^T(\chi, W) = \sum_{z_i \in D} \sum_{c \in SOM} K^T(\delta(c, \chi(z_i))) \|z_i - w_c\|^2$$

161 where $c \in SOM$ indices the neurons of the SOM map, χ is the allocation function that assigns
162 each element z_i of \mathbf{D} to its referent vector $w_{\chi(z_i)}$ and $\delta(c, \chi(z_i))$ is the discrete distance on the
163 SOM-map between a neuron c and the neuron allocated to observation z_i . K^T a kernel function
164 parameterized by T (where T stands for “temperature” in the scientific literature dedicated to
165 SOM) that weights the discrete distance on the map and decreases during the minimization
166 process. At the end of the learning process, the classification can be visualized onto the SOM-
167 map and interpreted in term of geophysics.

168 3.2 - Classification of the observations

169 In the present problem we chose to classify the annual cycles of the SST seasonal anomalies
170 observed in the Senegalo-Mauritanian upwelling. The study was made over the “extended
171 region” constituted of $25 \times 36 = 900$ pixels, but this enlarged region covers a part of the African
172 continent and 157 pixels are in fact over land. That means that we have truly 743 ocean pixels to deal
173 with. We consider the time-period of 30 years [1975 to 2005] extracted from the ERSST-V3b
174 database. For a given grid point and a given year and month, the monthly anomaly is the SST of



175 the pixel for which we have subtracted the mean of the considered year. The climatological mean
176 of the anomaly is then computed for each grid point by averaging each climatological month over
177 the 30 years. Thus, the learning data set \mathbf{D} is a set of 743 twelve-component vectors \mathbf{z} , each
178 component being the mean monthly anomaly computed as above. We denote “SST Seasonal
179 Cycle” the vector \mathbf{z} in the following.

180 We used a SOM-map to summarize the different SST seasonal cycles present in the "extended
181 region". We found that 120 prototypes (or neurons) can accurately represent the 743 vectors of \mathbf{D} .
182 This reduction (or vector quantization) is made by using a rectangular SOM-map of 30×4
183 neurons.

184 We then reduced the number of neurons in order to facilitate their interpretation in terms of
185 geophysical processes. For this, we applied a Hierarchical Ascendant Clustering algorithm
186 (HAC) using the Ward dissimilarity (Jain and Dubes, 1998). We grouped the 120 neurons into a
187 hierarchy that can contain between 120 and 1 clusters. Then the different classifications proposed
188 by the HAC were applied to the geographical region: each “SST Seasonal Cycle” of each grid
189 point of the region is assigned to a neuron and consequently to a cluster (assignment process),
190 thereby defining the so-called region-clusters. The problem is then to choose a number of clusters
191 that adequately synthesizes the geophysical phenomena over the region. This was done by
192 looking at the different possible classifications and choosing one representing the major
193 characteristics of the upwelling region. In [Fig. 2a](#), we observe that when we partition the SOM in
194 7 clusters, the associated 7 region-clusters are constituted of contiguous pixels in the geographic
195 map, and that two clusters (6, 7) are within the upwelling region and present a well-marked
196 seasonal cycle. For each region-cluster, we can estimate the associated standard deviations (STD
197 hereinafter) by processing all the data assigned to its associated neurons with a standard statistic
198 algorithm. The typical SST climatological cycles for each region-cluster are presented in [Fig. 2b](#)
199 together with their related error bars. We note that the region-clusters are well identified, their
200 typical climatological annual cycles of SST anomalies being well separated. Furthermore, the 7
201 region-clusters are spatially coherent and have a definite geophysical significance.

202 For the extended region under study, 7 therefore appears to be an adequate cluster number, since
203 this number allows a clear partition of the clusters on the HAC decision tree on the one hand, and
204 permits to assign a clear physical significance to each region-cluster on the other hand. Let us



205 now describe these clusters according to their physical significance with respect to the
206 geographical region: the Senegalo-Mauritanian coastal upwelling is associated with clusters 7 and
207 6. Cluster 2 corresponds to deep tropical waters associated with the equatorial Countercurrent.
208 Cluster 1 corresponds to surface waters of the Gulf of Guinea. Cluster 3 corresponds to the
209 offshore tropical Atlantic, and cluster 5 has extratropical characteristics. Cluster 4 is transition
210 between 3 and 5. As expected, the equatorial regions (clusters 1 and 2) have a very weak seasonal
211 cycle, which increases towards the extratropics (clusters 3 to 5). The upwelling regions (clusters
212 6 and 7) are characterized by an exceptionally strong seasonal variability.

213 **3.3 – Analysis of the different climate models**

214 The aim is now to find the model(s) that best fit the “Observation field”. A heuristic
215 manner is to compare the pattern of the different region-clusters of the CMIP5 models with
216 respect to those of the “Observation field” through a sight evaluating process. This kind of
217 approach has been proposed in (Sylla et al., 2019), and one indeed immediately sees that some
218 models better fit the “Observation field” than others. But this method remains very subjective.

219 In the following, we present a more objective approach. We use the previous
220 classification to objectively estimate how each CMIP5 model represents the “Observation field”
221 and its seven region-clusters. For this, we projected the SST annual cycle of each CMIP5 model
222 grid point of the extended region onto the SOM learned with the observations (section 3.2) using
223 the assignment procedure described in this section. Each grid point thus corresponds to a cluster
224 of the SOM and is represented on the geographical map by its corresponding color. Doing so, we
225 can represent each CMIP5 model by the geographical pattern of the 7 clusters partitioning the
226 SST seasonal cycle of its grid points. The geographical maps representing the 47 models and
227 their associated clusters are plotted in [Fig. 3](#). This graphical visualization is easier to compare
228 than the original characteristics (amplitude and phase) of the annual cycle at each grid point of a
229 model since each grid point can only take one discrete value among seven. This representation
230 immediately allows identifying the model biases and the models that best reproduce the cluster-
231 regions identified in the observations.

232 For a more quantitative assessment, we counted the number of grid points of a region-
233 cluster for a given CMIP5 model matching the same region-cluster of the “Observation field”.
234 We then computed the ratio between that matching number and the number of pixels of the



235 region-cluster of the considered model. That number is noted in the color-bar for each region-
236 cluster in [Fig. 3](#). We denote R_{mi} the ratio for the region-cluster i and the model m , where
237 $i = 1, \dots, 7$ is the number of the region-cluster and $m = 1, \dots, 47$ is the number of the model (see
238 table 1). We note that $R_{mi} \leq 1$. Doing so, each model m is represented by a 7-dimensional vector
239 R_m , each component being the ratio of a region-cluster. We estimated the total skill of a model
240 by averaging the 7 ratios. Note that this procedure gives the same weight to each region-cluster
241 whatever its number of grid point and its proximity with the upwelling region. In the following
242 the skill is presented as a percentage, the higher the skill, the better the fit. In [Fig. 3](#), the 47
243 CMIP5 models are ranked by their total skill, which is indicated above each panel beside the
244 model name. The model skills are very diverse, ranging from 79% to 28%. This Fig. also shows
245 that the models presenting the best total skill are also those representing thoroughly the upwelling
246 region. Some models represent the large-scale structure in the eastern tropical Atlantic (region-
247 clusters 3, 4, 5) very well but not the upwelling (33-GISS-E2-R and 34-GISS-E2-R-CC for
248 example). Others represent pretty well the upwelling region-clusters (region-clusters 6 and 7), but
249 not the large-scale structures of the SST seasonality (13-CSIRO-Mk-3-6-0, 6-CMCC-CESM for
250 example). None of this type of models is ranked among the best models, let us say with a score of
251 more than 60%. As indicated above, this representation gives a very synthetic view of the
252 structure of the seasonality of the SST in each of the models, potentially a very useful guide for
253 climate modelers to identify rapidly major biases.

254

255 **3.4 – Categorical analysis of the CMIP5 climate models**

256 In order to further progress in the selection of the models, the 47 climate models and the
257 Observation field were then analyzed by using a Multiple Correspondence Analysis (MCA in the
258 following). MCA is a multivariate statistical technique that is conceptually similar to principal
259 component analysis (PCA in the following), but applies to categorical rather than continuous
260 data. Similarly as PCA, it provides a way of displaying a set of data in a two-dimensional
261 graphical form. In the following, we applied a MCA analysis to the (47×7) matrix $R = [R_{mi}]$
262 whose elements represent the skills of the clusters of the models shown in front of the color bars
263 in [Fig. 3](#): the rows represent the different models, the columns the seven region-clusters. We
264 found that the first two principal axes of the MCA provide 71% of inertia. In [Fig. 4](#), we show a



265 projection of the models on the plane defined by the first two principal axes (each model being
266 represented by a small circle). Moreover, we projected the observation field (green diamond) on
267 that plane as a supplementary individual. The shorter the distance between two models, the more
268 similar the distribution of their region-cluster skills. On that plan, the seven clusters of the
269 observation field are represented by purple squares. Proximity between a model and a region-
270 cluster leads us to affirm that this region-cluster is well represented by that model. Clearly, some
271 models adequately represent the southern part of the extended region (region-clusters 1, 2 or 3),
272 where the SST seasonal cycle is weak, and are very distant from the upwelling regions (region-
273 cluster 6 and region-cluster 7) whose large SST cycle is poorly reproduced. In this group of
274 models, one recognizes the model 16-IPSL-CM5A-MR, at the extreme bottom of [Fig. 4](#), close to
275 region-clusters 4 and 5, consistently with [Fig. 3](#). At the other end of this group of models, the
276 model 23-HadCM3 for example is located very close to the region-cluster 1. [Fig. 3](#) indeed shows
277 that most of its grid points over the region of interest have a seasonal cycle resembling the one
278 found in the offshore tropical ocean. Another group of models is located in the center of this plan,
279 thus at an optimal distance of each of the observed regions-clusters, and not far from the overall
280 position of the observations (diamond). We recognize in this group of models, those that have a
281 high skill in [Fig. 3](#). The positioning of the observations (diamond in [Fig. 4](#)) with respect to the
282 models indeed allows selecting those that best represent the Observations field. The
283 representation given in [Fig. 4](#) allows understanding the drawback of the different models with
284 respect to the 7 Modes of SST-cycles.

285 As indicated in the introduction, the main objective of the methodology is to select an
286 ensemble of models that represents at best the upwelling behavior with respect to the
287 observations and to use this ensemble to predict the impact of climate change in the Senegalo-
288 Mauritanian upwelling with some confidence. The problem is now to determine a subset of
289 models that can adequately represent the observations, as the number of models is small enough
290 we choose to cluster them by HAC according to their projections onto the seven axes provided by
291 the MCA, and select the optimal jump in the hierarchical tree (Jain and Dubes, 1998).

292 Doing so, we obtain four homogeneous groups which are well separated (group 1, 2, 3, 4).
293 They are plotted with different colors in [Fig. 4](#). Clearly, the models are clustered with respect to
294 the region-clusters they best represent. We denote Model-group 1, Model-group 2, Model-group



295 3, Model-group 4 these multi-model ensembles hereinafter. Model-group 4 represents the
296 observations and the upwelling region-clusters at best.

297 For each group, we computed a multi-model average whose outputs are the mean of the
298 outputs of its different members and we analyzed it according to the same procedure (projection
299 of the SST-seasonal Cycle and assignment to a region-cluster) used for each individual model.
300 Besides we introduced the full multi-model average (Model-All in the following), which is the
301 multi-model ensemble which averages the 47 CMIP5 model outputs. Model-All was also projected
302 in the MCA plane and it is represented by a red star in Fig. 4. Comparison of the four model-groups
303 with Model-All and the observations are presented in Fig. 5. This figure visually highlights the
304 dominance of Model-group 4 for the reconstruction of the SST seasonal cycles of the different
305 region-clusters for the extended region. This is particularly clear for region-clusters 6 and 7,
306 which are those located in the upwelling region (Fig. 2). Model-group 3 seems to group models
307 characterized by an equatorward shift of the main structures, since the region-cluster 1 of tropical
308 waters is not reproduced and Region-clusters 4 and 5 of extratropical waters are overestimated.
309 Fig. 4 indeed shows that this Model-group is very close to the Regions-clusters 4 and 5, which
310 correspond to the extratropical and the transition geographical regions. Model-group 2
311 misrepresents the region of the Canary upwelling. Model-group 1 overestimates the SST seasonal
312 cycle in all the tropical open Atlantic. These two last model-groups overestimate the region-
313 Cluster 1, again consistently with their position in Fig. 4. A detailed physical interpretation of the
314 Model-groups is nevertheless beyond the scope of this paper. Clearly Model-All represents the
315 SST seasonal cycle of the off-shore ocean, but it proposes a very poor representation of the
316 upwelling region.

317 Two models (models 7 and 25) have a better skill than Model-group 4 and Model-All.
318 These two models are very close to the observations on the first two axes of the MCA (Fig 4). It
319 is easily seen that Model-group 4 and the projection of Model-All on this plane is farther than
320 that of model 7 and model 25 from the observation projection. This explains the lower
321 performance of these two multi-models as compared to models 7 and 25. In the present case, the
322 method permits to determine the best models (model 7 and model 25) and to outline the best
323 multi-model (Model-group 4) whose skill is better than any model with a probability of 95%
324 (number of models whose skill is smaller than the skill of Model-group 4 with respect to the total



325 number of models). Projection of the models on the other planes of the MCA analysis should
326 confirm this interpretation. One could then question the use of Model-group 4 rather than model
327 7 or model 25 individually. Furthermore, we argue that multi-model averages are in general more
328 robust for all sorts of climate studies than the use of a single model that can have good
329 performance for a very specific set of constraints but not for neighboring ones. The following
330 section will partly justify this point.

331 **4 - Classification of the climate models over a zoomed upwelling region**

332 The classification presented above relies largely on the ability of the models to represent
333 the off-shore seasonal cycle of the SST. In the following, we propose to test the classification
334 over a much more reduced area in order to focus the analysis on the upwelling area. This
335 “zoomed upwelling region” is shown in [Fig. 1](#). As for the extended region, we partitioned the
336 observations of the zoomed upwelling region with a SOM (ZSOM in the following) followed by
337 a HAC. We obtained new region-clusters denoted ZRegion-clusters. [Fig. 6](#) shows the four
338 ZRegion-clusters obtained from ERSSTv3b observations together with their associated mean
339 SST-Seasonal Cycle. Again, the ZRegion-clusters are spatially coherent. The upwelling area is
340 now decomposed into three ZRegion-clusters (ZRegion-clusters 2, 3, 4). This new decomposition
341 thus refines the study performed for the extended region: ZRegion-cluster 1 represents the
342 offshore ocean: its grid points typically have a SST seasonal cycle amplitude of 4°C, very similar
343 to Region-cluster 4 in the classification performed over the extended region ([Fig. 2](#)). ZRegion-
344 cluster-4 nicely identifies the core of the Senegalo-Mauritanian region, with grid points
345 characterized by the greatest amplitude of the SST seasonal cycle of the domain: typically 6.5°C.
346 It is interesting to note that an additional upwelling ZRegion-cluster (ZRegion-cluster 3) appears
347 south of ZRegion-cluster 4. Indeed, several studies have shown that the Cape Verde peninsula,
348 located around 15°N, separates the upwelling region into two distinct areas having a different
349 behavior north and south of this peninsula (Sirven et al. sub.,(Sylla et al., 2019)). The location of
350 the separation between ZRegion-cluster 3 and 4 is determined with some uncertainty due to the
351 coarse resolution (1°) of the ocean models. ZRegion-cluster 3 is marked by a time shift of the
352 seasonal cycle: the warmest season seems to occur somewhat one month earlier than in the other
353 regions as clearly seen in [Fig. 6](#) (left panel, yellow curve in June). Due a classification done in a much
354 larger region, such characteristic does not appear in the study over the extended area study. The



355 physical interpretation of the SST seasonal cycle of this ZRegion-cluster is beyond the scope of
356 the present study, but one can suspect a role of the ITCZ seasonal migration, covering these grid
357 points earlier than further north. Finally, ZRegion-cluster 2 is a transition between the large scale
358 ocean and the upwelling region. As for the extended region, we applied a MCA analysis to the
359 (47×4) matrix $R = [R_{mi}]$ whose elements represent the skills of the four clusters (i) of the 47
360 models. This MCA was followed by a HAC leading the definition of five ZModel-groups. The
361 members of each group are given in appendix. [Fig. 7](#) shows the ZRegion-cluster obtained in the
362 zoomed area by projecting these five ZModel-groups and Model-All model on the ZSOM and
363 their associated performances. ZModel-group 1 is the least performing one: only 25% of the grid
364 cells fall in the same class as for the observations. The structure of this model-group shows that it
365 is characterized by an homogeneous amplitude of the seasonal cycle over the whole domain,
366 suggesting a largely reduced upwelling: only one grid point at the coast has an enhanced SST
367 seasonal cycle as compared to the large scale tropical ocean. ZModel-group 2 is the best
368 performing one: 66% of the grid points are assigned to the correct class and the general picture
369 indeed represents a four-class picture fairly consistent with the observed structure ([Fig. 6](#)).
370 Important biases yet remain. In particular, the ZRegion-clusters 2 and 4 characterizing the
371 upwelling extend too far offshore. The three other ZModel-groups are intermediate. A relatively
372 reduced upwelling area, with an underestimated SST seasonal cycle, characterizes ZModel-
373 groups 3 and 4. ZModel-group 5 corresponds to a shift of the upwelling region towards the north.
374 Model-All also shows a strongly reduced seasonal cycle, with a large amount of pixel in the
375 intermediate ZRegion-cluster 3 and very few in the ZRegion-cluster 4. The ZRegion-cluster 3
376 representing the southern part of the Senegalo-Mauritanian upwelling does not appear in the
377 pattern of Model-All.

378 We remark that all the models forming ZModel-group 2 are included in Model-group 4.
379 For a more precise assessment, we can also project the entire Model-group 4, identified as the
380 best multi-model ensemble over the extended region, on the ZSOM ([Fig. 8](#), right). We notice that
381 the performance of Model-group 4 remains very high on this projection, indicating some
382 robustness of this multi-model ensemble. Moreover, this ensemble now outperforms the single
383 best model identified over the extended region ([Fig. 8](#), right). This result gives further confidence
384 in the use of multi-model averages, illustrating that one single model can be very skillful over a



385 specific region, or for a specific analysis, but multi-model averages are more robust across
386 various analysis and/or regions.

387 **5 – Impact of climate change on the Senegalo-Mauritanian upwelling**

388 **5.1 Representation of the upwelling in the CMIP5 climate models clusters**

389 In this section, we compare the representation of the Senegalo-Mauritanian upwelling system
390 given by the two best Model-groups identified above (Model-group 4 and ZModel-group 2). For
391 this evaluation, we use two of the five indices used by (Sylla et al., 2019) to evaluate the full
392 database, namely the intensity of the SST seasonal cycle and the offshore Ekman transport at the
393 coast. The former is specific to the seasonal variability of the Senegalo-Mauritanian upwelling
394 system, and it has been used for the classification. The latter is more general and although it has
395 recently been shown to partly represent the volume of the upwelled waters (Jacox et al., 2018), it
396 is extensively used in the scientific literature to characterize upwelling regions (Cropper et al.,
397 2014; Rykaczewski et al., 2015; Wang et al., 2015). Note also that following (Sylla et al., 2019),
398 evaluation is performed on the period [1985-2005]. This period slightly differs from the
399 classification period but the SST seasonal cycle is not significantly different (not shown).

400 Fig. 9 compares the amplitude of the SST seasonal cycle as represented in the
401 observations, Model-All, Model-group 4 and ZModel-group 2 identified above. Consistently with
402 Fig. 5 and 7, Model-All dramatically underestimates the upwelling signature in terms of SST
403 seasonal cycle as compared to the observations. Model-group 4 and ZModel-group 2 yield
404 improved results: the area of enhanced SST seasonal cycle is larger both in latitude and
405 longitude, with stronger SST amplitude values. This confirms the efficiency of the selection
406 operated above. Nevertheless, ZModel-group 2 yields a realistic SST amplitude pattern along the
407 coast but it extends too far offshore. Furthermore, in ZModel-group 2, the subtropical area (in
408 green in Fig 9) extends too far towards the south, in particular in the western part of the basin.
409 The tropical area, characterized by limited amplitude of the seasonal (deep blue in Fig. 9), is
410 shifted to the south as compared to the observations. In other words, the large scale thermal, and
411 thus probably dynamical structure of the region is poorly represented in ZModel-group 2. Finally,
412 Model-group 4 is the least biased one.



413 The intensity of the wind stress parallel to the coast, inducing offshore Ekman transport
414 and consequently an Ekman pumping at the coast, is generally considered as the main driver of
415 the upwelling. We therefore also tested the representation of this driver in the different Model-
416 groups. The idea is to evaluate the impact of the model selection performed above on the
417 representation of an independent variable by the Model-groups. Fig. 10 shows the latitude-time
418 evolution of the meridional oceanic wind stress, considering that the coast in the studied region is
419 oriented approximately meridionally, so that the offshore Ekman transport is mainly zonal. Note
420 that in Fig. 10, southward winds have positive values so that they correspond to a westward
421 Ekman transport, favorable to upwelling. Panel (a) shows that the observed meridional wind
422 stress is, all year long, favorable to the upwelling north of 20°N. At these latitudes, it is stronger
423 in summer. Between 12°N and 20°N, in the latitude band of the Senegalo-Mauritanian upwelling,
424 on the contrary, the wind blows southward with a very weak intensity in summer and it even
425 changes direction in the southern part of this latitude band. It is favorable to the upwelling in
426 winter-spring, which explains why the Senegalo-Mauritanian upwelling occurs during this season
427 with a maximum of intensity in March-April (Capet et al., 2017; Farikou et al., 2015). The main
428 bias of Model-All (Fig. 10b) is that the wind stress never reverses between 12°N and 20°N. It
429 weakens in the southern part of the Senegalo-Mauritanian latitude band, i.e. south of the Cape
430 Verde peninsula (15°N), but does not become negative. North of the Cape Verde peninsula, it
431 blows from the north also in summer, so that the Senegalo-Mauritanian upwelling lacks of
432 seasonality. This bias is corrected in Model-group 4 and ZModel-group 2 (Fig. 10 , panels c and
433 d) that are, in this aspect, more realistic than Model-All. Model-group 4 shows a slight extension
434 of the time and latitude range where the oceanic wind stress reverses sign. This constitutes an
435 improvement. The southward wind is nevertheless too strong in winter over the [12°N-20°N]
436 latitude band as well as further south from December to March. These two remaining biases are
437 further reduced in ZModel-group 2. This latter model yields the most realistic seasonal cycle of
438 meridional oceanic wind stress over the latitude band under study. This is consistent with a very
439 localized model selection, as the wind index is itself localized along the coast.

440 To conclude, Model-group 4 and ZModel-group 2 perform in general better than Model-All in
441 reproducing the major characteristic features of the Senegalo-Mauritanian upwelling. This result
442 confirms the relevance of the multi-model selection we have presented above. Applying the
443 methodology over a relatively large region allows to better constrain the spatial extent and pattern



444 of the SST signature of the upwelling than the reduced area. The latter however yields a better
445 representation of the wind seasonality along the coast.

446 **5.2 Response of the Senegalo-Mauritanian upwelling to global warming.**

447 In this section, we examine the response of the upwelling system given by the different
448 multi-model groups we selected, to global warming. For this, we compared the two indices
449 analyzed above in present-day and future conditions. The present-day conditions are taken as
450 above as the climatological average of historical simulations over the period [1985-2005]. The
451 future period is taken as the climatological average of the RCP8.5 scenario over the period [2080-
452 2100]. Fig. 11 shows the difference of the SST seasonal cycle amplitude between these two
453 periods. The general behavior is that the SST cycle amplitude will reduce in the upwelling region.
454 (Sylla et al., 2019) showed that this is primarily due to a warming of the winter temperature, thus
455 suggesting that the upwelling signature in surface will reduce. On the other hand, this figure
456 shows that the upwelling signature will increase along the Canary current, which flows along the
457 coast of Morocco, as well as in the subtropical part of our domain. This behavior is observed in
458 the three multi-model ensembles. Yet, the two selected Model-groups suggest a weaker decrease
459 of the SST seasonal cycle in the upwelling region than the one given by Model-All. ZModel-
460 group 2 shows an even weaker decrease mainly confined in the southern part of the upwelling
461 region. This result echoes findings of (Sylla et al., 2019) based on another indicator of the
462 upwelling imprint on the SST: they showed that the difference between the SST at the coast and
463 offshore is expected to decrease more in the southern part of the Senegalo-Mauritanian upwelling
464 system (SMUS) than in the north. We can hypothesize that the study conducted on the reduced
465 area permits to separate the Senegalo-Mauritanian upwelling system into two clusters, a northern
466 one (ZRegion 4) and a southern one (ZRegion-3) (Fig. 7) which enables to distinguish this
467 specific response.

468 The meridional wind stress also generally weakens under climate change in the [12°N-
469 20°N] latitude band (Fig. 12), suggesting a general reduction of the upwelling intensity. From
470 December to March, this is particularly true in the southernmost region of the Senegalo-
471 Mauritanian band, consistently with the results of (Sylla et al., 2019). The wind pattern inferred
472 from the two Model-groups (Fig. 12, middle and right panels) present a higher seasonal
473 variability than this of Model-All (left panel). The winter reduction of the southward wind stress



474 is slightly more confined to the southern region in ZModel-group 2, especially at the end of the
475 upwelling season (March-April) when the upwelling intensity is the strongest. This may be
476 consistent with the reduced seasonal cycle in the southernmost part of the upwelling identified
477 above.

478 **6 - Discussion and Conclusion**

479 This paper proposed an objective methodology for selecting climate models over a specific area
480 with respect to observations and according to well-defined statistical criteria. In the present study,
481 we have specifically checked the ability of the climate models to reproduce the ocean SST annual
482 cycle observed in specific regions of the studied area during the period 1975-2005 as reported in
483 the ERSST_v3b data set. These regions were defined by a neural classifier (SOM) as clusters
484 having similar seasonal SST cycles with respect to some statistical characteristics. They
485 correspond to ocean area having well marked oceanographic specificities.

486 We then checked the ability of the different climate models to reproduce the Region-clusters
487 defined on the observation dataset with a SOM. The better a climate model fits the clusters
488 computed with the SST observation, the better the skill of the model. We thus defined
489 geographical regions in the different CMIP5 climate models by projecting the SST annual cycle
490 of each model grid point onto the SOM. Each grid point is associated with a cluster on the SOM
491 map and consequently to a Region-cluster on the geographical map. We built an objective
492 similarity criterion by counting the number of grid points in a Region-cluster of a given
493 model matching the same Region cluster defined by processing the "Observation field". We
494 then computed the ratio between that matching number and the number of pixels of the Region-
495 cluster of the model under study. We estimated the total skill of a model by averaging the 7
496 ratios associated with the 7 Region clusters. Note that this procedure presents the advantage to
497 give the same weight to each region-cluster whatever its number of grid point and its proximity
498 with the upwelling region. This procedure respects the clustering done by the SOM since the
499 different clusters have an equal weight in the skill computation. In its present definition, the total
500 skill is a number between 0 and 1, the higher the skill, the better the fit. Other measures of the
501 total skill of a Model-group could nevertheless be defined depending on the objective of the
502 study.



503 Such a multi-model ensemble selection indeed allows subsampling a set of models in order to
504 obtain a more realistic climatology over the region of interest. The response of the upwelling to
505 climate change given by the different multi-model ensembles is quite robust in the sense that they
506 give similar qualitative answers. However, a too selective ensemble of models may lead to noisy
507 patterns. A compromise thus has to be found between the advantage of using a large number of
508 models, in order to smooth biases and unrealistic patterns, or selecting the most realistic models,
509 with the advantage of using a small number of models in the averaging procedure, but with the
510 possible inconvenience of getting spurious biases.

511 Different criteria have been used for selecting the best models included in the multi-model
512 ensemble used for climatic studies. The most common parameter is the average annual variability
513 in the surface mean temperature of the grid points of the region under study. Besides, (Knutti et
514 al., 2006) used the seasonal cycle in surface temperature represented by seasonal amplitude in
515 temperature calculated as summer June–August (JJA) minus winter December–February (DJF)
516 temperature. This criterion is more informative than the annual variability in the mean
517 temperature since the amplitude of the seasonal variability is an important criterion characterizing
518 the validity of a climate model. In the present work we used a much more informative criterion
519 which is formed of the monthly temperature cycle represented by a 12 component vector, each
520 component representing the average monthly temperature of the year we consider. This new
521 criterion allows taking account the amplitude and the phase of seasonal variability while the
522 (Knutti et al., 2006) criterion takes only into account the amplitude of the seasonal variability.
523 More generally, (Sylla et al., 2019) extensively discussed the possible differences among the
524 different indices aiming at characterizing the upwelling and the need to use several of them to
525 have a complete understanding of this costal phenomenon. This conclusion is probably general to
526 any physical process of the climate system. In the present study, the model selection is only based
527 on one signature of the SMUS. Ongoing studies in our group investigate the possibility of
528 merging several indices such as SST, wind intensity and direction, ocean currents,... This
529 approach could also allow a selection of models based on the representation of several distinct
530 regional processes.

531 Different applications of the multi-model selection strategy proposed in the present study can be
532 envisaged. Firstly, from a purely modeling point of view, the projection of the models on the



533 SOM (or ZSOM) and the results of the HAC yield a very enlightening description of a given
534 model behavior in terms of region-clusters of the area under study. In our view, such a procedure
535 could advantageously be used by individual modeling groups to identify, analyze and therefore
536 hopefully reduce their model biases in a targeted region. Secondly, from a physical point of view,
537 an identified Model-group can be used to analyze the targeted region (here the SMUS) in term of
538 processes with the advantages of the multi-model mean in which the constituting models have
539 been selected from objective criteria. Such an application has been briefly illustrated by showing
540 how the selected Model-group represents an important additional characteristic of the SMUS, not
541 used for the selection, namely the Ekman pumping. Promising reduction of biases of the full
542 multi-model mean ensemble has been identified, opening perspectives for process studies based
543 on this sub-ensemble of the CMIP5 database. A third application of the selection lies in the
544 prediction of the future climate. Here, we have shown that selected multi-model ensembles may
545 provide a more precise description of the future behavior of the SMUS. It may nevertheless be
546 important to note that these conclusions are based on the assumption that the CMIP5 models
547 which have been selected according to their present-day characteristics, are the most reliable in
548 terms of future projections, which can be questioned and refined (Lutz et al., 2016; Reifen and
549 Toumi, 2009).

550 As discussed in the introduction, “model democracy”, suggesting that all models should be
551 equally considered in multi-model ensemble is now strongly questioned (Knutti et al., 2017). The
552 present study proposes a promising way to improve the quality of multi-model ensemble in
553 terms of model selection. Deep advances in the field of multi-model analysis and selection can be
554 expected from the emerging topic of climate informatics (Monteleoni et al., 2013) as it has been
555 shown through the present study. Artificial intelligence and machine learning may indeed provide
556 efficient tools to progress in making the best out of the extraordinary but imperfect tools that are
557 the climate models and the multi-model intercomparison efforts.

558

559 **Acknowledgments**

560 NOAA_ERSST_V3b data provided by the NOAA/OAR/ESRL PSD, Boulder, Colorado, USA,
561 from their Web site at <https://www.esrl.noaa.gov/psd/> The research leading to these results has
562 received funding from the NERC/DFID Future Climate for Africa program under the SCUS-2050
563 project, emanating from **AMMA-2050** project, grant number NE/M019969/1. The authors also



564 acknowledge support from the Laboratoire Mixte International ECLAIRS2, supported by the
565 french Institut de Recherche pour le Développement. To analyze the CMIP5 data, this study
566 benefited from the IPSL Prodiguer-Ciclad facility which is supported by CNRS, UPMC, Labex
567 L-IPSL which is funded by the ANR (Grant #ANR-10-LABX-0018) and by the European FP7
568 IS-ENES2 project (Grant #312979)

569 **Code and Data availability:** The model output used for this study is feely available on the ESGF
570 database for example following this url: <https://esgf-node.ipsl.upmc.fr/search/cmip5-ipsl/>. The
571 SST data were downloaded from
572 <https://www.esrl.noaa.gov/psd/data/gridded/data.noaa.ersst.v3.html> and the winds data
573 here: <https://podaac.jpl.nasa.gov> . The code developed for the core computations of this study can
574 be found under: 10.5281/zenodo.3476724. This code allows reproducing Fig. 2, 3, 6, 7 and 8.

575 **Author contribution:** JM initially proposed the idea, ST and MC translated it in terms of
576 methodology and coordinated the method development, CS and CM developed the code and
577 produced the figure, CS, CM, MC, ST all contributed to the statistical analysis. AS provided the
578 initial definition of the upwelling index and performed the analysis under climate change that
579 appears in section 5. JM and MC prepared the manuscript with contributions from all the authors.

580

581

582

583



584 **APPENDIX**

585

Model-group 1	Model-group 2	Model-group 3	Model-group 4
ACCESS1-0 ACCESS1-3 CESM1-CAM5 CESM1-CAM5-1-FV2 CESM1-WACCM HadCM3 MIROC-ESM MIROC-ESM-CHEM MIROC5 NorESM1-M NorESM1-ME	bcc-csm1-1 bcc-csm1-1-m BNU-ESM CCSM4 CESM1-BGC CESM1-FASTCHEM GFDL-CM2p1 GFDL-ESM2G GFDL-ESM2M MPI-ESM-LR MPI-ESM-MR MPI-ESM-P	FGOALS-g2 GISS-E2-H GISS-E2-H-CC GISS-E2-R GISS-E2-R-CC inmcm4 IPSL-CM5A-LR IPSL-CM5A-MR IPSL-CM5B-LR MRI-CGCM3 MRI-ESM1	CanCM4 CanESM2 CMCC-CESM CMCC-CM CMCC-CMS CNRM-CM5 CNRM-CM5-2 CSIRO-Mk3-6-0 FGOALS-s2 GFDL-CM3 HadGEM2-AO HadGEM2-CC HadGEM2-ES

586

ZModel-group 1	ZModel-group 2	ZModel-group 3	ZModel-group 4
ACCESS1-0 bcc-csm1-1-m CCSM4 CESM1-BGC CESM1-CAM5 CESM1-CAM5-1-FV2 CESM1-FASTCHEM CESM1-WACCM GISS-E2-H GISS-E2-H-CC GISS-E2-R GISS-E2-R-CC HadCM3 inmcm4 IPSL-CM5B-LR MIROC5 MPI-ESM-LR MPI-ESM-MR MPI-ESM-P	CMCC-CMS CNRM-CM5 CNRM-CM5-2 FGOALS-s2 GFDL-CM3	BNU-ESM CanCM4 CanESM2 CMCC-CM FGOALS-g2 IPSL-CM5A-LR IPSL-CM5A-MR MRI-CGCM3 NorESM1-M NorESM1-ME	ACCESS1-3 bcc-csm1-1 CSIRO-Mk3-6-0 HadGEM2-AO HadGEM2-CC HadGEM2-ES MIROC-ESM MIROC-ESM-CHEM MRI-ESM1
			ZModel-group 5
			CMCC-CESM GFDL-CM2p1 GFDL-ESM2G GFDL-ESM2M

587

588 Table A1: Composition of the different Model-groups identified in the main text. In bold, we
 589 show the CMIP5 models which belong to Model-group 4 and ZModel-group 2. We note that all
 590 the models belonging to Zmodel-group 2 also belong to Model-group 4.



591 **REFERENCES**

- 592 Borodina, A., Fischer, E. M. and Knutti, R.: Emergent constraints in climate projections: A case
593 study of changes in high-latitude temperature variability, *J. Clim.*, 30(10), 3655–3670,
594 doi:10.1175/JCLI-D-16-0662.1, 2017.
- 595 Capet, X., Estrade, P., Machu, E., Ndoye, S., Grelet, J., Lazar, A., Marié, L., Dausse, D.,
596 Brehmer, P., Capet, X., Estrade, P., Machu, E., Ndoye, S., Grelet, J., Lazar, A., Marié, L.,
597 Dausse, D. and Brehmer, P.: On the Dynamics of the Southern Senegal Upwelling Center:
598 Observed Variability from Synoptic to Superinertial Scales, *J. Phys. Oceanogr.*, 47(1), 155–180,
599 doi:10.1175/JPO-D-15-0247.1, 2017.
- 600 Cox, P. M., Pearson, D., Booth, B. B., Friedlingstein, P., Huntingford, C., Jones, C. D. and Luke,
601 C. M.: Sensitivity of tropical carbon to climate change constrained by carbon dioxide variability,
602 *Nature*, 494(7437), 341–344, doi:10.1038/nature11882, 2013.
- 603 Cropper, T. E., Hanna, E. and Bigg, G. R.: Spatial and temporal seasonal trends in coastal
604 upwelling off Northwest Africa, 1981-2012, *Deep. Res. Part I Oceanogr. Res. Pap.*, 86, 94–111,
605 doi:10.1016/j.dsr.2014.01.007, 2014.
- 606 Deangelis, A. M., Qu, X., Zelinka, M. D. and Hall, A.: An observational radiative constraint on
607 hydrologic cycle intensification, *Nature*, 528(7581), 249–253, doi:10.1038/nature15770, 2015.
- 608 Demarcq, H. and Faure, V.: Coastal upwelling and associated retention indices derived from
609 satellite SST. Application to *Octopus vulgaris* recruitment, *Oceanol. Acta*, 23(4), 391–408,
610 doi:10.1016/S0399-1784(00)01113-0, 2000.
- 611 Farikou, O., Sawadogo, S., Niang, A., Diouf, D., Brajard, J., Mejia, C., Dandonneau, Y., Gasc,
612 G., Crepon, M. and Thiria, S.: Inferring the seasonal evolution of phytoplankton groups in the
613 Senegalo-Mauritanian upwelling region from satellite ocean-color spectral measurements, *J.*
614 *Geophys. Res. Ocean.*, 120(9), 6581–6601, doi:10.1002/2015JC010738, 2015.
- 615 Fasullo, J. T. and Trenberth, K. E.: A less cloudy future: The role of subtropical subsidence in
616 climate sensitivity, *Science* (80-.), 338(6108), 792–794, doi:10.1126/science.1227465, 2012.
- 617 Faye, S., Lazar, A., Sow, B. A. and Gaye, A. T.: A model study of the seasonality of sea surface
618 temperature and circulation in the Atlantic North-eastern Tropical Upwelling System, *Front.*



- 619 Phys., 3(September), 1–20, doi:10.3389/fphy.2015.00076, 2015.
- 620 Gao, Y., Lu, J. and Leung, L. R.: Uncertainties in projecting future changes in atmospheric rivers
621 and their impacts on heavy precipitation over Europe, *J. Clim.*, 29(18), 6711–6726,
622 doi:10.1175/JCLI-D-16-0088.1, 2016.
- 623 Gleckler, P. J., Taylor, K. E. and Doutriaux, C.: Performance metrics for climate models, *J.*
624 *Geophys. Res. Atmos.*, 113(6), D06104, doi:10.1029/2007JD008972, 2008.
- 625 Gordon, N. D., Jonko, A. K., Forster, P. M. and Shell, K. M.: An observationally based constraint
626 on the water-vapor feedback, *J. Geophys. Res. Atmos.*, 118(22), 12435–12443,
627 doi:10.1002/2013JD020184, 2013.
- 628 Hewitson, B. C. and Crane, R. G.: Self-organizing maps: Applications to synoptic climatology,
629 *Clim. Res.*, 22(1), 13–26, doi:10.3354/cr022013, 2002.
- 630 Huber, M. and Knutti, R.: Anthropogenic and natural warming inferred from changes in Earth’s
631 energy balance, *Nat. Geosci.*, 5(1), 31–36, doi:10.1038/ngeo1327, 2012.
- 632 Jacox, M. G., Edwards, C. A., Hazen, E. L. and Bograd, S. J.: Coastal Upwelling Revisited:
633 Ekman, Bakun, and Improved Upwelling Indices for the U.S. West Coast, *J. Geophys. Res.*
634 *Ocean.*, 1–19, doi:10.1029/2018JC014187, 2018.
- 635 Jain, A. K. and Dubes, R. C.: Algorithms for clustering data, Prentice Hall Advanced Reference
636 Serie, Englewood. Cliffs., 1998.
- 637 Jouini, M., Lévy, M., Crépon, M. and Thiria, S.: Reconstruction of satellite chlorophyll images
638 under heavy cloud coverage using a neural classification method, *Remote Sens. Environ.*, 131,
639 232–246, doi:10.1016/j.rse.2012.11.025, 2013.
- 640 Jouini, M., Béranger, K., Arsouze, T., Beuvier, J., Thiria, S., Crépon, M. and Taupier-Letage, I.:
641 The Sicily Channel surface circulation revisited using a neural clustering analysis of a high-
642 resolution simulation, *J. Geophys. Res. Ocean.*, 121(7), 4545–4567, doi:10.1002/2015JC011472,
643 2016.
- 644 Knutti, R., Meehl, G. A., Allen, M. R. and Stainforth, D. A.: Constraining climate sensitivity
645 from the seasonal cycle in surface temperature, *J. Clim.*, 19(17), 4224–4233,



- 646 doi:10.1175/JCLI3865.1, 2006.
- 647 Knutti, R., Furrer, R., Tebaldi, C., Cermak, J., Meehl, G. A., Knutti, R., Furrer, R., Tebaldi, C.,
648 Cermak, J. and Meehl, G. A.: Challenges in Combining Projections from Multiple Climate
649 Models, *J. Clim.*, 23(10), 2739–2758, doi:10.1175/2009JCLI3361.1, 2010.
- 650 Knutti, R., Sedláček, J., Sanderson, B. M., Lorenz, R., Fischer, E. M. and Eyring, V.: A climate
651 model projection weighting scheme accounting for performance and interdependence, *Geophys.*
652 *Res. Lett.*, 44(4), 1909–1918, doi:10.1002/2016GL072012, 2017.
- 653 Kohonen, T.: Essentials of the self-organizing map, *Neural Networks*, 37, 52–65,
654 doi:10.1016/j.neunet.2012.09.018, 2013.
- 655 Kounta, L., Capet, X., Jouanno, J., Kolodziejczyk, N., Sow, B. and Gaye, A. T.: A model
656 perspective on the dynamics of the shadow zone of the eastern tropical North Atlantic – Part 1:
657 the poleward slope currents along West Africa, *Ocean Sci.*, 14(5), 971–997, doi:10.5194/os-14-
658 971-2018, 2018.
- 659 Lambert, S. M. and Boer, G. J.: {CMIP1} evaluation and intercomparison of coupled climate
660 models, *Clim. Dyn.*, 17, 83–106, 2001.
- 661 Liu, Y., Weisberg, R. H. and Mooers, C. N. K.: Performance evaluation of the self-organizing
662 map for feature extraction, *J. Geophys. Res. Ocean.*, 111(5), C05018,
663 doi:10.1029/2005JC003117, 2006.
- 664 Loeb, N. G., Wang, H., Cheng, A., Kato, S., Fasullo, J. T., Xu, K.-M. and Allan, R. P.:
665 Observational constraints on atmospheric and oceanic cross-equatorial heat transports: revisiting
666 the precipitation asymmetry problem in climate models, *Clim. Dyn.*, 46(9–10), 3239–3257,
667 doi:10.1007/s00382-015-2766-z, 2015.
- 668 Lutz, A. F., ter Maat, H. W., Biemans, H., Shrestha, A. B., Wester, P. and Immerzeel, W. W.:
669 Selecting representative climate models for climate change impact studies: an advanced
670 envelope-based selection approach, *Int. J. Climatol.*, 36(12), 3988–4005, doi:10.1002/joc.4608,
671 2016.
- 672 Masson, D. and Knutti, R.: Climate model genealogy, *Geophys. Res. Lett.*, 38(8), n/a-n/a,
673 doi:10.1029/2011GL046864, 2011.



- 674 Monteleoni, C., Schmidt, G., Alexander, F., Niculescu-Mizil, A., Steinhäuser, K., Tippet, M.,
675 Banerjee, A., Blumenthal, M., Ganguly, A., Smerdon, J. and Tedesco, M.: Climate Informatics,
676 in Computational Intelligent Data Analysis for Sustainable Development, pp. 81–126., 2013.
- 677 Ndoye, S., Capet, X., Estrade, P., Sow, B. A., Dagonne, D., Lazar, A., Gaye, A. T. and Brehmer,
678 P.: SST patterns and dynamics of the southern Senegal-Gambia upwelling center, *J. Geophys.*
679 *Res. Ocean.*, 119(12), 8315–8335, doi:10.1002/2014JC010242, 2014.
- 680 O’Gorman, P. A., Allan, R. P., Byrne, M. P. and Previdi, M.: Energetic Constraints on
681 Precipitation Under Climate Change, *Surv. Geophys.*, 33(3–4), 585–608, doi:10.1007/s10712-
682 011-9159-6, 2012.
- 683 Phillips, T. J. and Gleckler, P. J.: Evaluation of continental precipitation in 20th century climate
684 simulations: The utility of multimodel statistics, *Water Resour. Res.*, 42(3),
685 doi:10.1029/2005WR004313, 2006.
- 686 Pincus, R., Batstone, C. P., Patrick Hofmann, R. J., Taylor, K. E. and Glecker, P. J.: Evaluating
687 the present-day simulation of clouds, precipitation, and radiation in climate models, *J. Geophys.*
688 *Res. Atmos.*, 113(14), doi:10.1029/2007JD009334, 2008.
- 689 Reichler, T. and Kim, J.: How well do coupled models simulate today’s climate?, *Bull. Am.*
690 *Meteorol. Soc.*, 89(3), 303–311, doi:10.1175/BAMS-89-3-303, 2008.
- 691 Reifen, C. and Toumi, R.: Climate projections: Past performance no guarantee of future skill?,
692 *Geophys. Res. Lett.*, 36(13), 1–5, doi:10.1029/2009GL038082, 2009.
- 693 Reusch, D. B., Alley, R. B. and Hewitson, B. C.: North Atlantic climate variability from a self-
694 organizing map perspective, *J. Geophys. Res. Atmos.*, 112(2), D02104,
695 doi:10.1029/2006JD007460, 2007.
- 696 Richardson, A. J., Risi En, C. and Shillington, F. A.: Using self-organizing maps to identify
697 patterns in satellite imagery, in *Progress in Oceanography*, vol. 59, pp. 223–239, Pergamon.,
698 2003.
- 699 Rykaczewski, R. R., Dunne, J. P., Sydeman, W. J., García-Reyes, M., Black, B. A. and Bograd,
700 S. J.: Poleward displacement of coastal upwelling-favorable winds in the ocean’s eastern
701 boundary currents through the 21st century, *Geophys. Res. Lett.*, 42(15), 6424–6431,



- 702 doi:10.1002/2015GL064694, 2015.
- 703 Santer, B. D., Taylor, K. E., Gleckler, P. J., Bonfils, C., Barnett, T. P., Pierce, D. W., Wigley, T.
704 M. L., Mears, C., Wentz, F. J., Bruggemann, W., Gillett, N. P., Klein, S. A., Solomon, S., Stott,
705 P. A. and Wehner, M. F.: Incorporating model quality information in climate change detection
706 and attribution studies, *Proc. Natl. Acad. Sci.*, 106(35), 14778–14783,
707 doi:10.1073/pnas.0901736106, 2009.
- 708 Sawadogo, S., Brajard, J., Niang, A., Lathuiliere, C., Crépon, M. and Thiria, S.: Analysis of the
709 Senegalo-Mauritanian upwelling by processing satellite remote sensing observations with
710 topological maps., in *Proceedings of the International Joint Conference on Neural Networks*, pp.
711 2826–2832, IEEE., 2009.
- 712 Smith, T. M., Reynolds, R. W., Peterson, T. C. and Lawrimore, J.: Improvements to NOAA’s
713 historical merged land-ocean surface temperature analysis (1880–2006), *J. Clim.*, 21(10), 2283–
714 2296, doi:10.1175/2007JCLI2100.1, 2008.
- 715 Son, S. W., Gerber, E. P., Perlwitz, J., Polvani, L. M., Gillett, N. P., Seo, K. H., Eyring, V.,
716 Shepherd, T. G., Waugh, D., Akiyoshi, H., Austin, J., Baumgaertner, A., Bekki, S., Braesicke, P.,
717 Brühl, C., Butchart, N., Chipperfield, M. P., Cugnet, D., Dameris, M., Dhomse, S., Frith, S.,
718 Garny, H., Garcia, R., Hardiman, S. C., Jöckel, P., Lamarque, J. F., Mancini, E., Marchand, M.,
719 Michou, M., Nakamura, T., Morgenstern, O., Pitari, G., Plummer, D. A., Pyle, J., Rozanov, E.,
720 Scinocca, J. F., Shibata, K., Smale, D., Teyssdre, H., Tian, W. and Yamashita, Y.: Impact of
721 stratospheric ozone on Southern Hemisphere circulation change: A multimodel assessment, *J.*
722 *Geophys. Res. Atmos.*, 115(19), D00M07, doi:10.1029/2010JD014271, 2010.
- 723 Stegehuis, A. I., Vautard, R., Ciais, P., Teuling, A. J., Jung, M. and Yiou, P.: Summer
724 temperatures in Europe and land heat fluxes in observation-based data and regional climate
725 model simulations, *Clim. Dyn.*, 41(2), 455–477, doi:10.1007/s00382-012-1559-x, 2013.
- 726 Sylla, A., Mignot, J., Capet, X. and Gaye, A. T.: Weakening of the Senegalo–Mauritanian
727 upwelling system under climate change, *Clim. Dyn.*, 1–27, doi:10.1007/s00382-019-04797-y,
728 2019.
- 729 Tan, I., Storelvmo, T. and Zelinka, M. D.: Observational constraints on mixed-phase clouds
730 imply higher climate sensitivity, *Science (80-)*, 352(6282), 224–227,



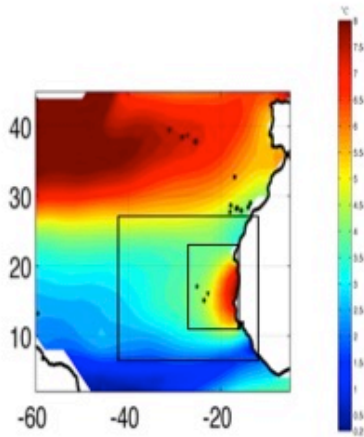
- 731 doi:10.1126/science.aad5300, 2016.
- 732 Taylor, K. E., Stouffer, R. J. and Meehl, G. A.: An Overview of CMIP5 and the Experiment
733 Design, *Bull. Am. Meteorol. Soc.*, 93(4), 485–498, doi:10.1175/BAMS-D-11-00094.1, 2012.
- 734 Tebaldi, C. and Knutti, R.: The use of the multi-model ensemble in probabilistic climate
735 projections, *Philos. Trans. R. Soc. A Math. Phys. Eng. Sci.*, 365(1857), 2053–2075,
736 doi:10.1098/rsta.2007.2076, 2007.
- 737 Wang, D., Gouhier, T. C., Menge, B. A. and Ganguly, A. R.: Intensification and spatial
738 homogenization of coastal upwelling under climate change, *Nature*, 518(7539), 390–394,
739 doi:10.1038/nature14235, 2015.
- 740 Wenzel, S., Cox, P. M., Eyring, V. and Friedlingstein, P.: Emergent constraints on climate-
741 carbon cycle feedbacks in the CMIP5 Earth system models, *J. Geophys. Res. Biogeosciences*,
742 119(5), 794–807, doi:10.1002/2013JG002591, 2014.
- 743 Wenzel, S., Eyring, V., Gerber, E. P. and Karpechko, A. Y.: Constraining future summer austral
744 jet stream positions in the CMIP5 ensemble by process-oriented multiple diagnostic regression, *J.*
745 *Clim.*, 29(2), 673–687, doi:10.1175/JCLI-D-15-0412.1, 2016.
- 746
- 747



nb	Model Acronym	nb	Model Acronym
1	bcc-csm1-1	25	HadGEM2-ES
2	bcc-csm1-1-m	26	MPI-ESM-LR
3	BNU-ESM	27	MPI-ESM-MR
4	CanCM4	28	MPI-ESM-P
5	CanESM2	29	MRI-CGCM3
6	CMCC-CESM	30	MRI-ESM1
7	CMCC-CM	31	GISS-E2-H
8	CMCC-CMS	32	GISS-E2-H-CC
9	CNRM-CM5	33	GISS-E2-R
10	CNRM-CM5-2	34	GISS-E2-R-CC
11	ACCESS1-0	35	CCSM4
12	ACCESS1-3	36	NorESM1-M
13	CSIRO-Mk3-6-0	37	NorESM1-ME
14	inmcm4	38	HadGEM2-AO
15	IPSL-CM5A-LR	39	GFDL-CM2p1
16	IPSL-CM5A-MR	40	GFDL-CM3
17	IPSL-CM5B-LR	41	GFDL-ESM2G
18	FGOALS-g2	42	GFDL-ESM2M
19	FGOALS-s2	43	CESM1-BGC
20	MIROC-ESM	44	CESM1-CAM5
21	MIROC-ESM-CHEM	45	CESM1-CAM5-1-FV2
22	MIROC5	46	CESM1-FASTCHEM
23	HadCM3	47	CESM1-WACCM
24	HadGEM2-CC		

748

749 Table 1: List of the CMIP5 models used for the comparison. The reader is referred to the CMIP5
 750 documentation for more information on each of them. Here, each configuration is furthermore
 751 given a number, for easier identification in subsequent figures.
 752



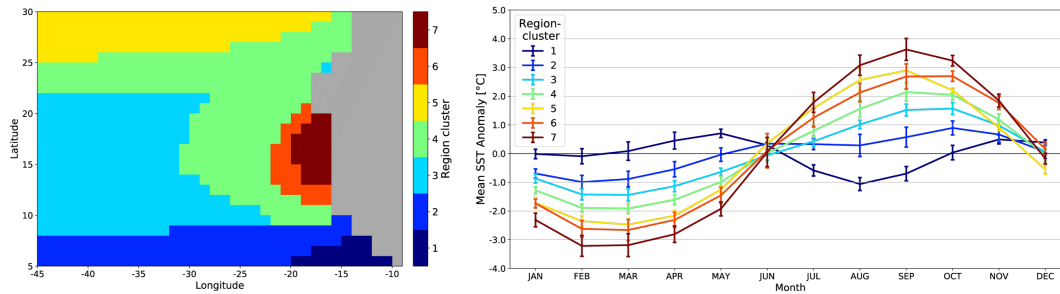
753

754

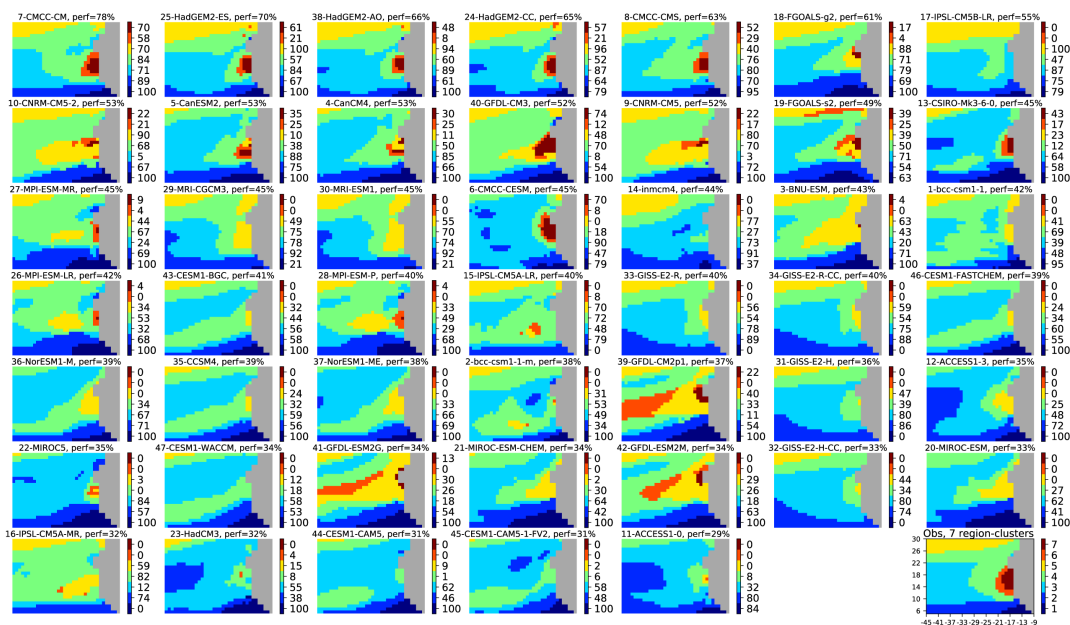
755 Figure 1: Amplitude of the SST seasonal cycle in the western tropical north Atlantic. SST data
756 are from the ERSSTv3b data set averaged between 1975 and 2005. The two black boxes show the
757 extended and zoomed regions respectively over which the statistical classifications were
758 performed (see text for details).
759



760



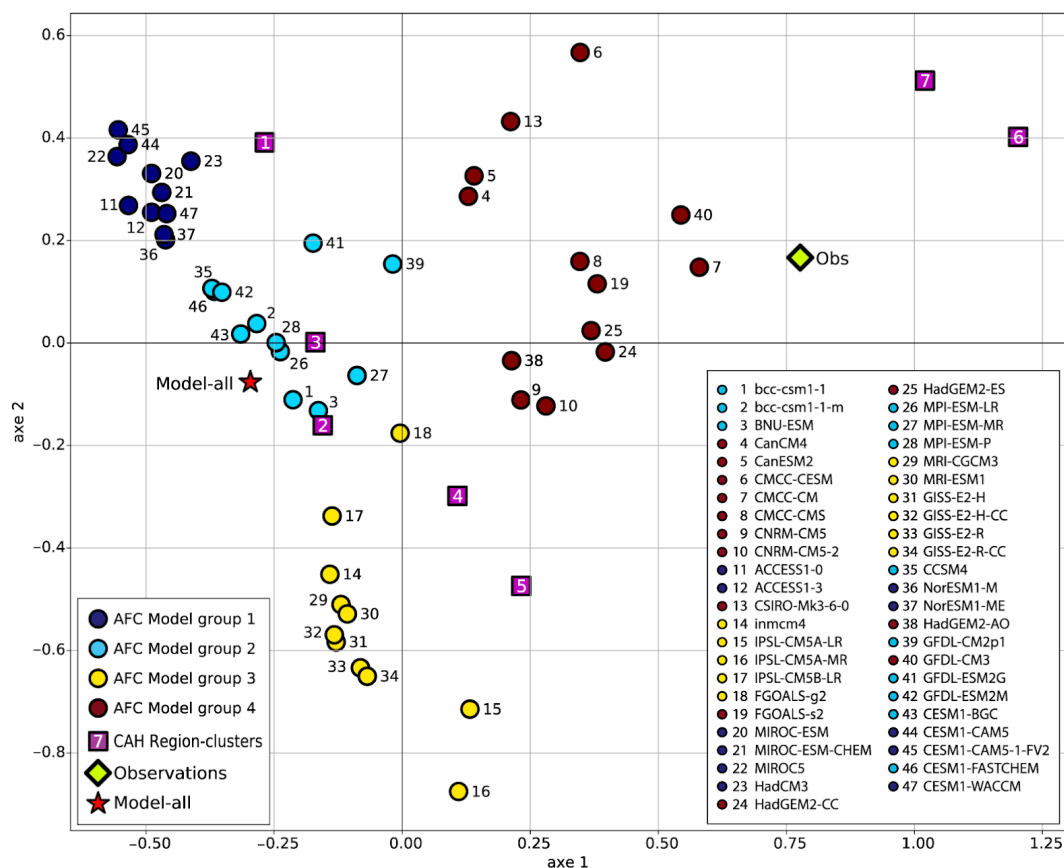
761 Figure 2: Left panel: Region-clusters associated with the SOM-clusters obtained after a HAC on
762 a 30x4 neuron SOM learned on ERSSTv3b observations in the extended zone (see text for
763 details). Right Panel: Ensemble-mean climatological SST cycles for the grid points of the seven
764 Region-clusters. The error bars show the standard deviation of this ensemble mean.
765



766

767

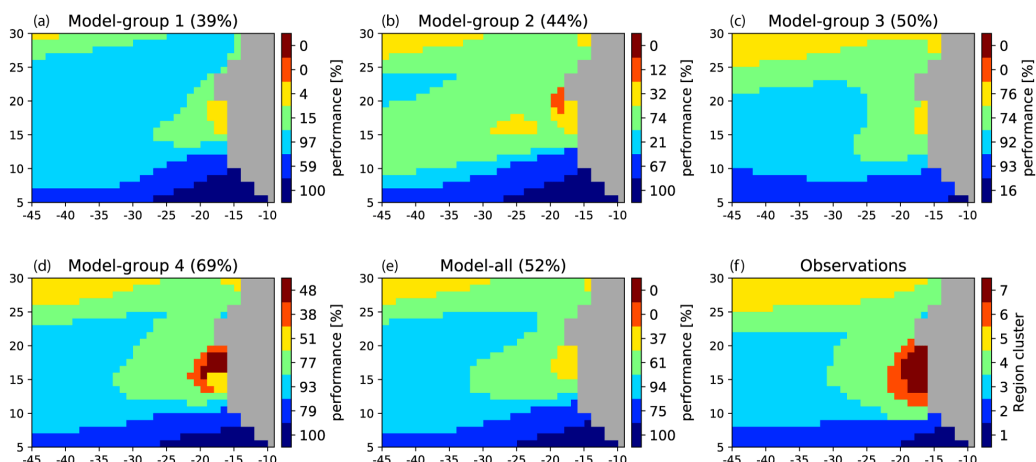
768 Figure 3: Projection of the 47 climate models of the CMIP5 database onto the SOM learned with
 769 ERSSTv3b climatology in the extended zone (see Fig. 1). On top of each panel, we figure: the
 770 number referencing the model, its name (Table 1), and its skill given as a mean percentage (see
 771 text). The models are ordered according to their skill in decreasing order. The 7 Region-clusters
 772 (or SOM-clusters) are defined by applying an HAC to the SOM output learned with the
 773 observation field. They are represented by different colors. The numbers in the colorbar at the
 774 right of each panel represent the skill for each Region-cluster. The observation field is shown in
 775 the bottom right panel and the numbers in front of the colorbar reference the Region-cluster.
 776



777

778 Figure 4: Projection of the CMIP5 models (colored circles) and the observation field (green
 779 green diamond) defined by their cluster skill vectors on the first two axis of the MCA. The seven
 780 region-clusters of the observation field are represented by purple squares. The colours of the
 781 circles denote the four groups of models obtained after an HAC was performed on the seven
 782 MCA components of the models. The projection of the full multi-model mean (47 models) is
 783 represented by a red star.

784

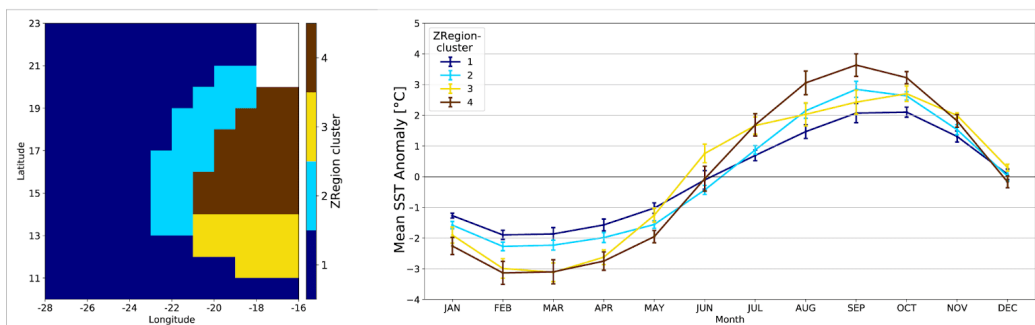


785

786 Figure 5: (a)-(d): Projection of the multi-model ensembles (Model-group) onto the SOM learned
787 with ERSSTv3b climatology in the extended zone. Multi-model ensemble performances are
788 obtained by averaging the skill of the models forming each group. The performances are given
789 on top of each panel. The Region-clusters determined by processing the observations in the
790 extended area and their associated colors are given in the bottom right panel. The colorbars at the
791 right of each multi-ensemble panel represent the skill (in %) associated with each Region-cluster.
792 Panel (e) shows the same for the full multi-model ensemble. Panel (f) reproduces the Region-
793 clusters based on the observations also shown in Fig. 2.

794

795



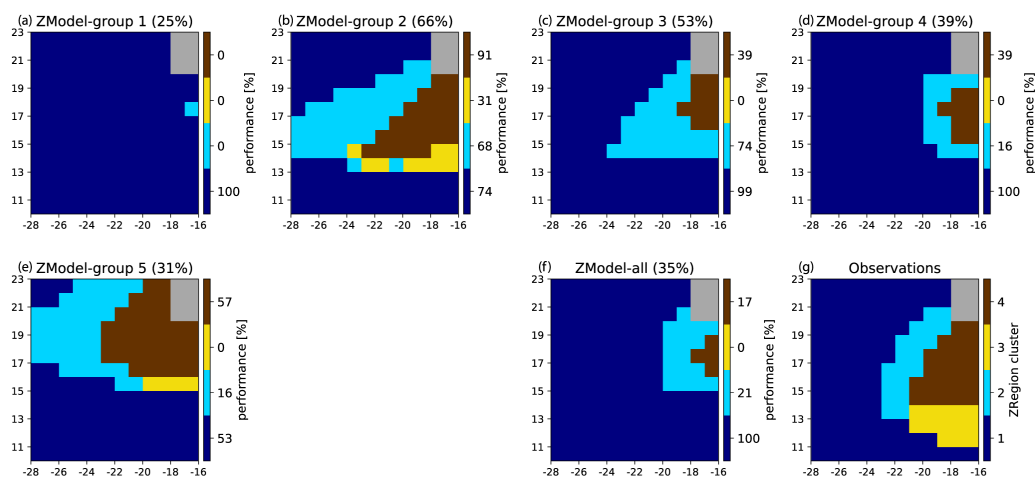
796

797 Figure 6: Left panel: ZRegion-clusters associated with the ZSOM-clusters obtained after a HAC
798 on a 10x12 neuron SOM learned on ERSSTv3b observations in the zoomed zone (see text for
799 details). Right Panel: Ensemble-mean climatological SST cycles for the grid points of the four
800 ZRegion-clusters. The error bars show the standard deviation of this ensemble mean.

801

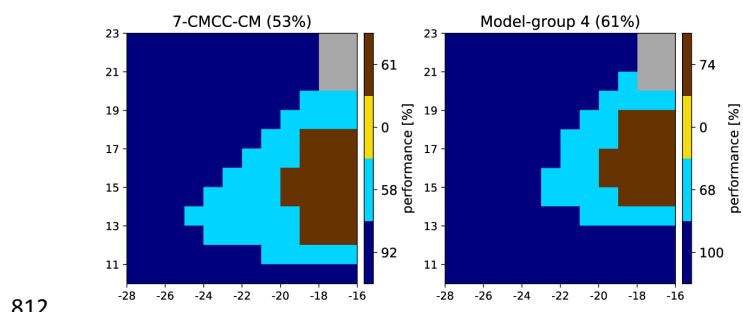
802

803



804

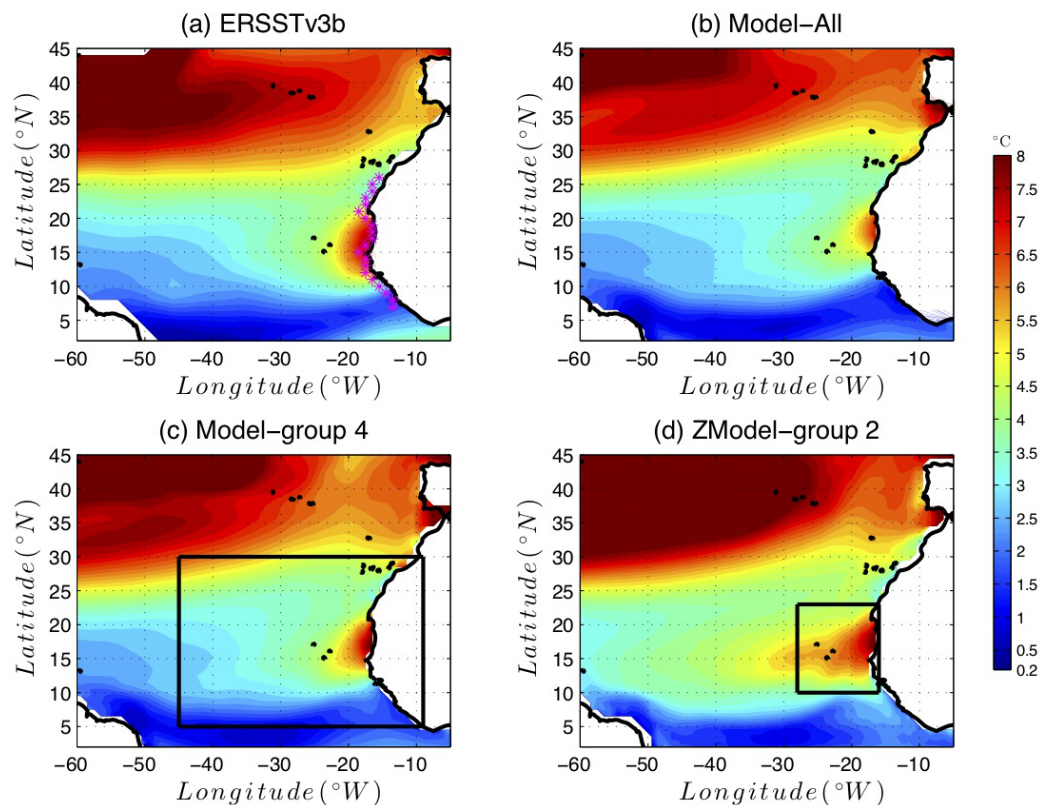
805 Figure 7: (a)-(e): Projection of the multi-model ensembles (ZModel-groups) onto the ZSOM.
806 The performances are given on top of each panel. The ZRegion-clusters determined by processing the
807 observations in the zoomed region and their associated colors are given in the bottom right panel.
808 The colorbars at the right of each multi-ensemble panel represent the skill (in %) associated with
809 each ZRegion-cluster. Panel (f) shows the same for the full multi-model ensemble. Panel (g)
810 reproduces the Region-clusters based on the observations also shown in Fig. 6.
811



812

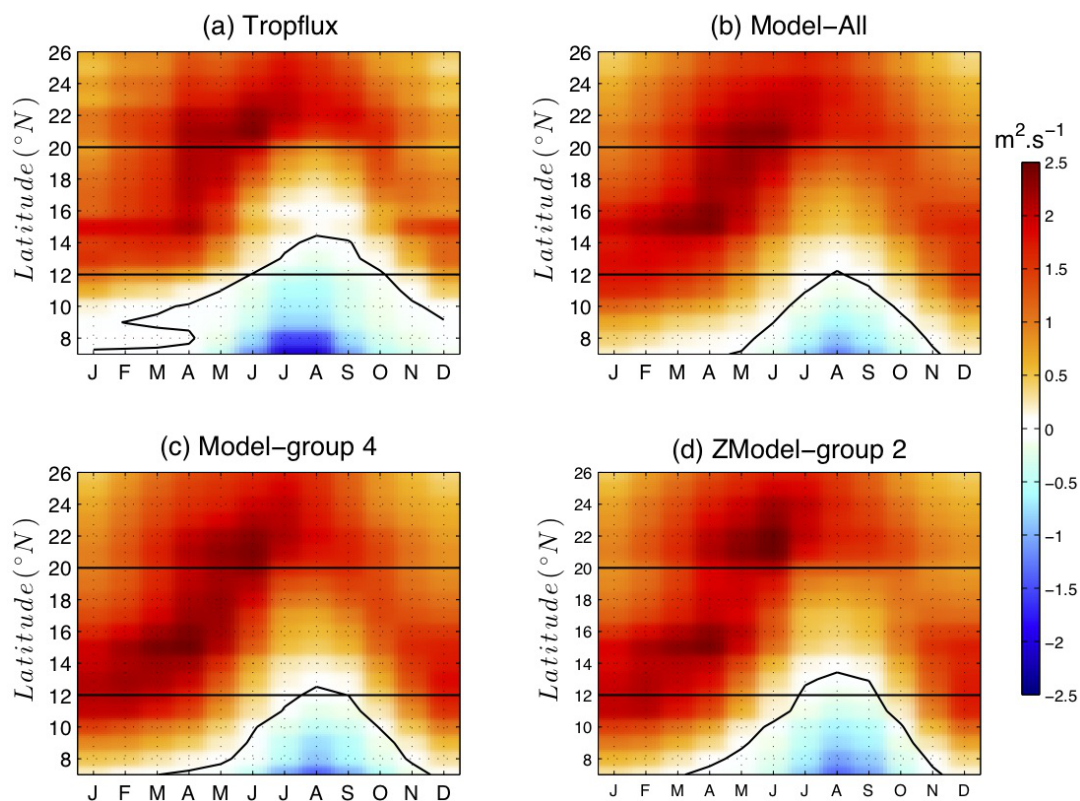
813 Figure 8 : Same as Fig. 7 but for the individual model CMCC-CM (model 7) (left) and the
814 Model-group 4 (right).

815



816

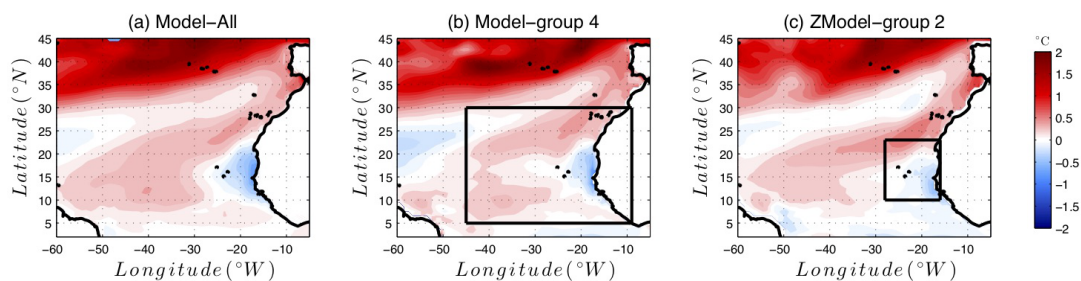
817 Figure 9: Amplitude of the SST seasonal cycle in the (a) ERSSTv3b Observations (b) Model-All,
818 (c) Model-group 4 (best Model-group for the extended area, figured out by the black rectangular
819 box) and (d) ZModel-group 2 (best Model-group for the reduced area, figured out by the small
820 black rectangular box). The SST seasonal cycle is computed over the period 1985-2005
821



822

823 Figure 10: Latitude-time plot of depth integrated Ekman transport computed over the grid point
824 located along the coast (magenta stars in Fig. 9.a). The time axis shows climatological months
825 over the period 1985-2005. Positive (negative) values correspond to upwelling (downwelling)
826 conditions. Panel (a) stands for TropFlux data set (see Praveen Kumar et al. (2013) (b) Model-
827 All, (c) Model-group 4 and (d) ZModel-group 2. On each panel, the black contour shows the
828 contour zero. The horizontal dashed lines are positioned at 12°N and 20°N and give a rough
829 limitation of the senegalo-mauritanian upwelling region.
830

831

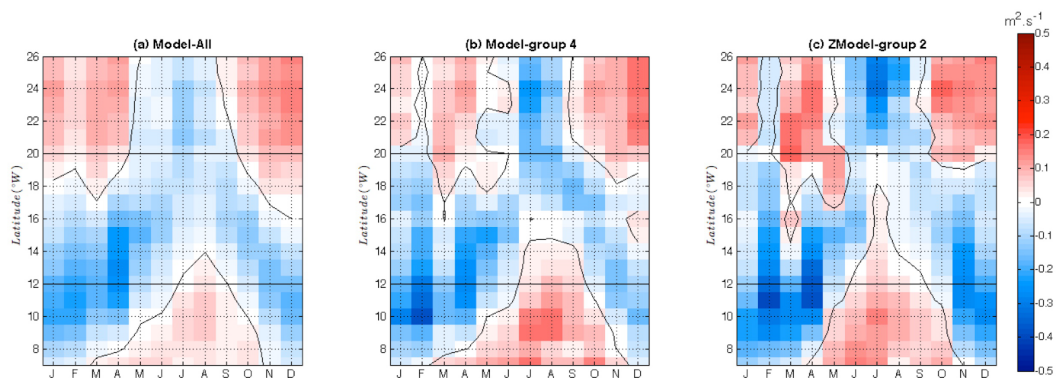


832

833 Figure 11: Evolution of the amplitude of the SST seasonal cycle at the end of the 21st century.
834 The figure shows the difference between the seasonal cycle amplitude averaged over the period
835 [2080-2100] following the RCP8.5 scenario and the amplitude averaged over the period [1985-
836 2005] in the historical simulations. A positive value (red) means that the seasonal cycle is more
837 marked over the period 2080-2100.

838

839



840

841 Figure 12: Latitude-time diagram of the seasonal shift of the meridional component of the wind-
842 stress with respect to the present days. For each month and at each latitude, we show the
843 meridional wind stress shift with respect to the present days averaged over the period [2080-
844 2100]. Positive values (red) means that the wind stress shift is southward and is thus favorable to
845 upwelling. Panel (a) stands for Model-All, (b) Model-group 4 and (c) ZModel-group 2.
846